

Investigation on Crack Propagation Mechanisms in Surrounding Rock Induced by Excavation Unloading of Deep-Buried Caverns

Donghan Wang^{2,3}, Kaiwen Song^{2,3}, Qian Dong¹ and Junhong Huang^{2,3}

¹Hubei Key Laboratory of Blasting Engineering, Wuhan, China

²Sanya Science and Education Innovation Park, Wuhan University of Technology, Sanya Hainan, China

³School of Civil Engineering and Architecture, Wuhan University of Technology, Wuhan Hubei, China

Keywords: Rock Mechanics, Numerical Simulation, Roadway Surrounding Rock, Transient Unloading, Small-Scale Surrounding Rock Specimens.

Abstract: To investigate the deformation patterns and failure mechanisms of roadway surrounding rock under transient excavation unloading, and to simulate the roadway excavation unloading process, a model test system for roadway excavation and unloading was developed. Multiple sets of jointed rock mass model specimens were fabricated using high-strength gypsum materials. Numerical simulations were employed to explore the influences of joint quantity, length, stiffness, and spatial configuration on the failure characteristics of surrounding rock during excavation unloading. The results indicate that under transient unloading conditions: Jointed rock masses exhibit a higher degree of failure compared to intact rock masses. Rock masses containing longer joints demonstrate more pronounced failure phenomena than those with shorter joints. Joint stiffness exerts relatively minor influence on both peripheral displacement and damage extent of the excavation. Rock masses with mixed-length joints show greater susceptibility to failure compared to those with uniform-length joints. Multi-jointed rock masses are more prone to crack formation during unloading, potentially leading to more significant rock deformation and crack propagation. In contrast, rock masses with fewer joints experience less impact under such transient unloading conditions, consequently demonstrating enhanced stability and safety of the surrounding rock.

1 INTRODUCTION

To prevent geotechnical hazards in deep rock mass engineering, such as roadway instability and rockbursts, a deeper understanding of the interaction mechanisms between surrounding rock and support structures is imperative. Previous studies predominantly focused on interpreting rock unloading phenomena through loading theories. However, stress release induced by roadway excavation is the primary cause of the loosened zone in surrounding rock, necessitating consideration of the mechanical properties of both rock mass and support structures under varying stress states during excavation unloading. International research on excavation unloading commenced earlier. For instance: Cai et al., 2007 simulated damage distribution characteristics in surrounding rock during deep tunnel excavation using software like PFC. In China: Lu et al., 2008 proposed and validated the concept of transient unloading during excavation through mechanical analysis and duration

calculations of load release. Lu et al., 2008 identified excavation unloading as the primary cause of large-scale damage zones in surrounding rock.

Research on deep rock mass excavation unloading characteristics initially focused on classical theoretical mechanics and numerical simulations, supplemented by theoretical analyses of practical engineering issues. Key findings include: Luo et al., 2023 analyzed the post-unloading mechanical states and deformation behaviors of rock masses using classical mechanics. Dong et al., 2017 investigated the impacts of initial in-situ stress, excavation radius, and dynamic rock strength on unloading-induced failure and stability. Dong et al., 2017 demonstrated that the extent of surrounding rock failure correlates strongly with unloading duration, with shorter durations inducing greater disturbance magnitudes.

Instantaneous excavation unloading induces vibrations and failure in rock masses. Through case studies, Fan et al., 2015 and Lu et al., 2007 found that larger unloading volumes during excavation result in stronger vibrations, and transient unloading

may amplify the overall vibration response of surrounding rock.

Current research on dynamic excavation unloading primarily focuses on the dynamic response of rock masses. To investigate crack propagation mechanisms in both jointed and intact rock masses under excavation unloading, this study designed laboratory model tests and numerical simulations, followed by systematic analysis of the results.

2 SIMULATION TEST SYSTEM FOR LOOSENING OF UNDERGROUND CAVERN STRUCTURAL PLANES UNDER TRANSIENT EXCAVATION UNLOADING

This section analyzes surrounding rock stress distribution, introduces a self-developed testing system, and integrates theoretical-experimental methodology to establish foundations for subsequent lab tests.

2.1 Stress Distribution of Roadway Surrounding Rock

To elucidate the stress distribution of surrounding rock in semi-circular arched roadways with vertical walls and predict their failure patterns, the following analytical approaches are conducted:

The stress distribution of roadway surrounding rock constitutes a plane strain problem, which can be solved using the complex variable method (2018; Zhu et al., 2014; Dai & Zhang, 2012). The in-situ stress field of semi-circular arched roadways with vertical walls comprises vertical stress σ_V , horizontal stress σ_H , and shear stress τ . The surrounding rock stress can be expressed by two complex potential functions: $\varphi(z)$, and $\psi(z)$.

$$\begin{cases} \varphi(z) = \frac{\sigma_1^0 + \sigma_3^0}{4} \omega(\xi) + \varphi_0(\xi) \\ \psi(z) = -\frac{1}{2}[(\sigma_1^0 - \sigma_3^0)e^{-2i\alpha} \omega(\xi) + \psi_0(\xi)] \end{cases} \quad (1)$$

Parameters $\varphi_0(\xi)$, $\psi_0(\xi)$, and $\omega(\xi)$ in Equation (1) are determined, while σ_1^0 and σ_3^0 are assigned according to Equation (2):

$$\begin{cases} \sigma_1^0 = \frac{\sigma_V + \sigma_H}{2} + \sqrt{\left(\frac{\sigma_V - \sigma_H}{2}\right)^2 + (\tau_{HV})^2} \\ \sigma_3^0 = \frac{\sigma_V + \sigma_H}{2} - \sqrt{\left(\frac{\sigma_V - \sigma_H}{2}\right)^2 + (\tau_{HV})^2} \\ \alpha = \arctan\left(\frac{\sigma_V - \sigma_H}{2\tau_{HV}} + \sqrt{\left(\frac{\sigma_V - \sigma_H}{2\tau_{HV}}\right)^2 + 1}\right) \end{cases} \quad (2)$$

Consequently, the stress distribution of roadway surrounding rock is derived as:

$$\begin{cases} \sigma_\rho + \sigma_\theta = 4 \operatorname{Re} \left(\frac{\varphi'(\xi)}{\omega'(\xi)} \right) \\ \sigma_\rho - \sigma_\theta + 2i\tau_{\rho\theta} = \frac{2\xi^2}{\rho^2} \left[\frac{\overline{\omega(\xi)}}{\omega'(\xi)} \left(\frac{\varphi'(\xi)}{\omega'(\xi)} \right)' + \frac{\psi'(\xi)}{\omega'(\xi)} \right] \end{cases} \quad (3)$$

2.2 Introduction to the Test System

To intuitively investigate the deformation behavior of jointed rock masses during instantaneous excavation unloading, a simulation test system for transient unloading-induced loosening of structural planes in underground caverns was designed. The system operates as follows:

(I) Mechanical Configuration

The front end of a lever-type loading/unloading assembly is embedded into the pre-excavated slot within the surrounding rock model (containing structural planes) and tightly contacts the slot wall. The rear end is connected to a suction-cup electromagnetic actuator via a welded cylindrical steel tube.

(II) Unloading Simulation Process

Under axial tensile loading, the lever mechanism applies controlled interfacial pressure to the slot wall in the chamber assembly. Deactivating the electromagnetic actuator triggers instantaneous pressure release, simulating transient stress-field unloading (Figure 1). This system facilitates lab-scale simulation of excavation loading/unloading cycles, with the lever mechanism enabling instantaneous structural plane unloading in pre-excavated models through controlled energy storage/release.

In terms of material selection, gypsum is adopted for rock mass modeling due to its ease of processing, customizable composition, and cost-effectiveness. Gypsum-based materials remain widely utilized in dynamic rock experiments. Dimensions and physical characteristics of the surrounding rock specimens are detailed in Figure 2.

The model incorporates centrally positioned pre-existing cracks with mica sheets embedded along vertically penetrating surfaces to simulate primary

structural planes in surrounding rock. A roadway excavation of standardized geometry is implemented at the specimen's center to improve real-world scenario simulation fidelity.

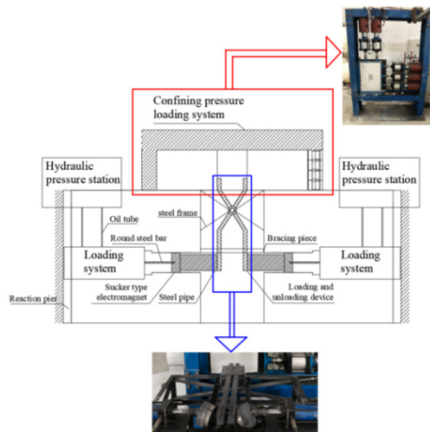


Figure 1: Schematic diagram of simulation test system.

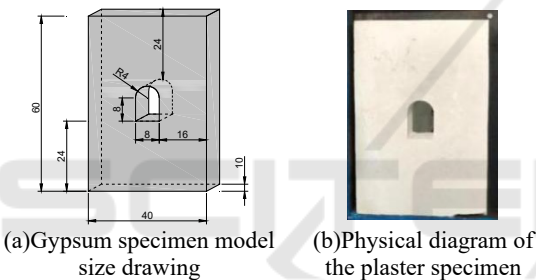


Figure 2: Size drawing and physical drawing of surrounding rock specimen.

3 DESIGN OF LABORATORY TESTS FOR TRANSIENT UNLOADING DURING DEEP-BURIED CAVERN EXCAVATION

3.1 Uniaxial Compressive Strength Testing of Gypsum

Gypsum was selected as the surrounding rock simulation material for subsequent tests. To determine the compressive strength of the gypsum material used in the tests, uniaxial compression tests were conducted using a 50 kN microcomputer-controlled electronic universal testing machine (Figure 3). The standard cylindrical specimens (Figure 4) measured 50 mm in diameter and 100 mm in height. A loading rate of 5 mm/min was applied to

ensure complete acquisition of stress-strain curves. Photographs of five specimens before and after failure are summarized in Table 1, with corresponding stress-strain curves presented in Fig. 5.

Accounting for material heterogeneity and experimental errors, the average uniaxial compressive strength and elastic modulus of the gypsum material were determined as 3.92 MPa and 5.77 GPa, respectively. This section must be in two columns.

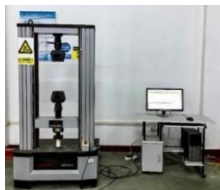


Figure 3: Physical diagram of experimental equipment.

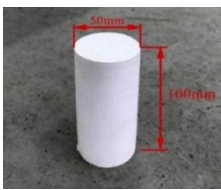


Figure 4: Dimensions of test standard parts.

Table 1: Typical photographs of standard gypsum specimens before and after uniaxial compression failure..

Pre-failure	Post-failure	Pre-failure	Post-failure

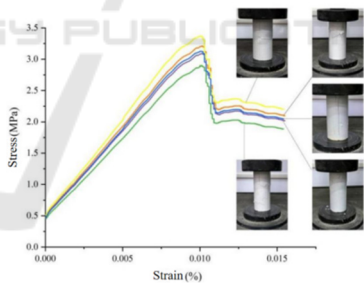
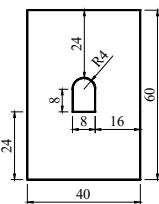
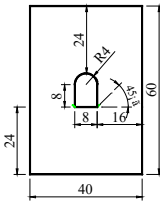
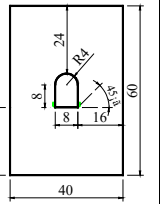
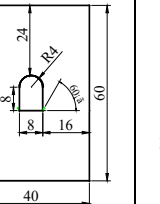
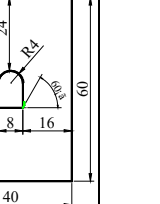
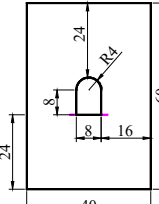
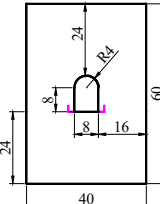
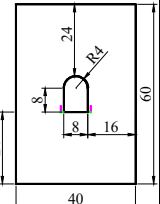
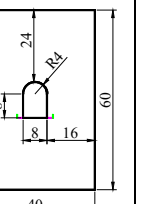
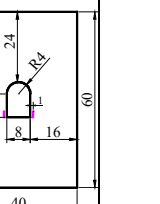
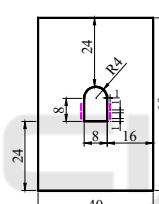
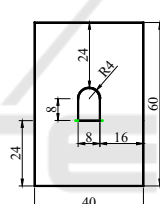
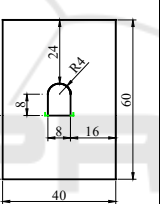
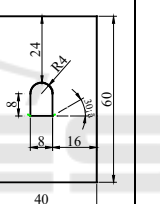


Figure 5: Stress-strain curves of gypsum specimens.

3.2 Experimental Methodology

The simulation test system (Section 2.1) applied 2 MPa confining pressure with instantaneous unloading ($\leq 0.5s$). Mica-embedded gypsum specimens with variable joint geometries (quantity/length/orientation) simulated excavation-induced structural planes. Fourteen test groups (Table 2) captured systematic crack propagation patterns near discontinuities, providing empirical validation for structural plane evolution mechanisms under excavation unloading disturbances.

Table 2: Schematic diagram of test conditions.

Schematic Diagram					
	Test Case 1 (Without mica sheets)	Test Case 2 (Two 1 cm mica sheets)	Test Case 3 (Four 1 cm mica sheets)	Test Case 4 (Two 1 cm mica sheets)	Test Case 5 (Four 1 cm mica sheets)
Schematic Diagram					
	Test Case 6 (Two 2 cm mica sheets)	Test Case 7 (Four 2 cm mica sheets)	Test Case 8 (Two 1 cm and two 2 cm mica sheets)	Test Case 9 (Two 1 cm and two 2 cm mica sheets)	Test Case 10 (Two 2 cm mica sheets)
Schematic Diagram					
	Test Case 11 (Four 2 cm mica sheets)	Test Case 12 (Two 1 cm mica sheets)	Test Case 13 (Four 1 cm mica sheets)	Test Case 14 (Two 1 cm mica sheets)	

3.3 Analysis of Recorded Experimental Phenomena

Post-test documentation and analysis of gypsum failure characteristics were conducted as follows:


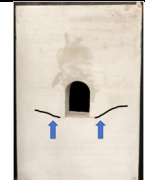

3.3.1 Failure Characteristics of Intact and Jointed Rock Masses

A comparative analysis of intact rock masses (Test Case 1) and jointed rock masses (represented by Test Cases 6 and 12) before and after testing is presented in Table 3. To enhance visibility of experimental phenomena, crack trajectories in the images were manually highlighted with black lines to accentuate fine fractures that were otherwise difficult to discern.

Experimental observations showed intact rock under high confining pressure exhibited plastic deformation with gradual microcrack development and eventual fracture, while sudden unloading induced elastic recovery that reduced plasticity and

accelerated crack dilation. In contrast, jointed rock masses demonstrated reduced integrity due to pre-existing discontinuities, causing localized stress concentrations and accelerated crack propagation under equivalent loading, resulting in extended cracks and more pronounced failure phenomena.

Table 3: Phenomena of unjointed rock mass and partially jointed rock mass after failure.

Test Case 1	Test Case 6	Test Case 12
		

3.3.2 Failure Characteristics of Jointed Rock Masses with Varying Properties

(I)Different Joint Lengths
Comparative analysis indicates 2 cm-jointed rock masses exhibit longer post-unloading cracks than 1 cm-jointed counterparts due to reduced transient stress concentrations near joint planes in shorter joints, enhancing stability and limiting crack propagation.

Table 4: Diagram of post-failure phenomena at different joint lengths.

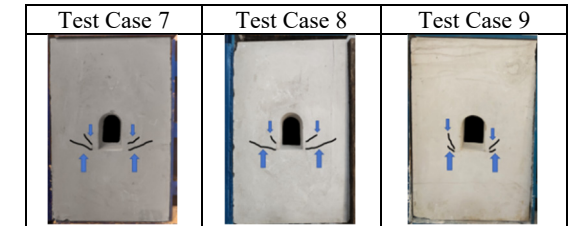
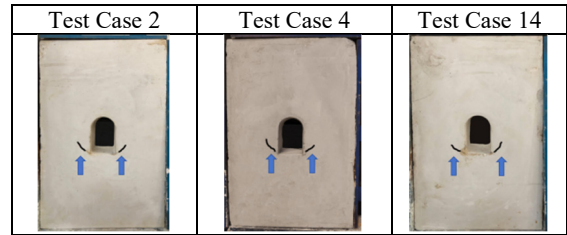


Figure 6: Schematic diagram of the naming of mica sheets.

Table 6: Diagram of the phenomenon after failure at different joint dip angles.



Test Cases 3/5/13 (Table 7) with four mica sheets each demonstrated that steeper dip angles of No.② mica sheet ($45^{\circ}/60^{\circ}/0^{\circ}$) inversely correlated with No. ① mica sheet proximity to excavation boundaries (Case 13>3>5). Post-test analysis revealed crack coalescence between mica sheets and excavation boundaries in Case 5 but no crack initiation along No. ① sheet in Case 13. Proximity to excavations reduces confinement, enabling transient unloading-induced crack formation, while distant fractures under higher confinement exhibit suppressed crack initiation/propagation.

Table 7: Diagram of the post-failure phenomenon of different joint dip angles.

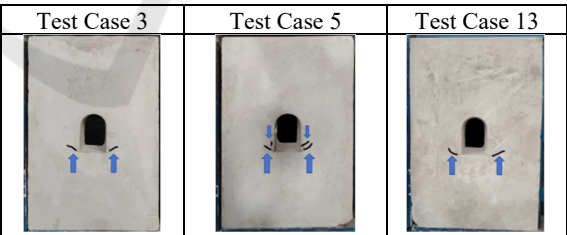
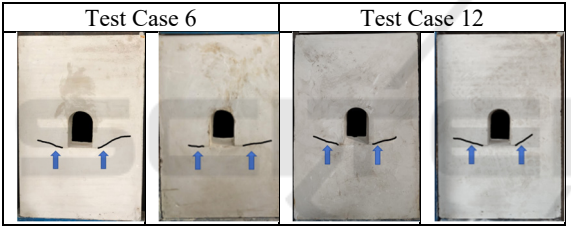


Table 5: Diagram of post-failure phenomena at different joint lengths.



Mixed-length joints exhibit compound transient failure: longer joints initiate fracturing as shorter joints amplify damage, reducing safety margins versus uniform joints during dynamic excavation (Table 4, Table 5).

(II)Different Joint Dip Angles
Table 6 documents failure progression in specimens with 1 cm mica sheets at 30° , 45° , 60° dip angles (Cases 2/4/14) under transient unloading. Mica sheets are spatially indexed per Figure 6 for precise damage characterization.

Comparative analysis of Test Cases 2, 4, and 14 revealed that under identical joint lengths and transient unloading conditions: Cracks exhibited comparable lengths and predominantly propagated along joint planes. Increasing joint dip angles resulted in steeper crack trajectories (i.e., greater angles relative to the horizontal).

(III)Different Joint Numbers

Table 8: Phenomena after failure of different joint quantities.

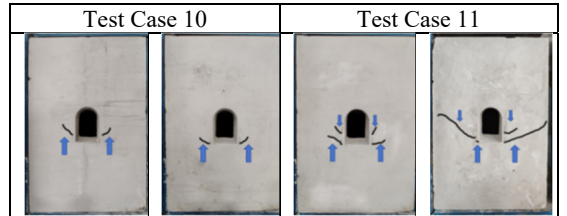


Table 8 demonstrates crack-joint quantity proportionality: Multi-jointed systems near excavation boundaries undergo simultaneous joint propagation-deformation-cracking processes under transient unloading, where adjacent joint interactions amplify rock deformation/crack coalescence, substantially destabilizing rock masses. Fewer-joint configurations exhibit diminished joint interplay and unloading sensitivity, yielding superior stability/safety through restricted crack development.

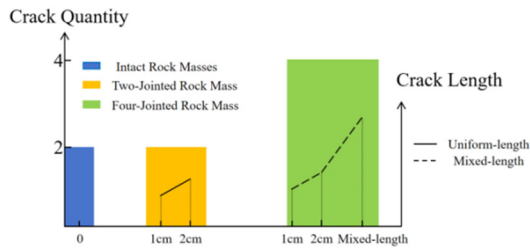


Figure 7: Correspondence Between Joint and Crack Dimensions: Lengths and Quantities.

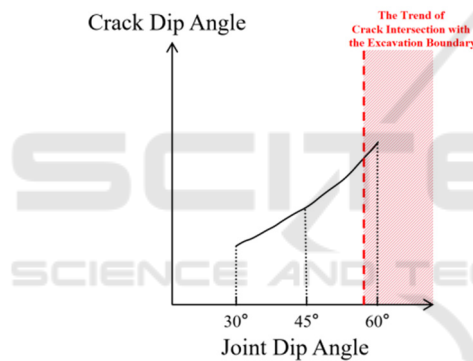


Figure 8: Relationship between Joint Dip Angles and Crack Trajectories.

Experimental results (Figures 7, 8) demonstrate intact rock masses generate fewer cracks than jointed counterparts under transient unloading. Increased joint quantity directly elevates crack numbers in single-length jointed systems. Equivalent joint quantities show steeper Joint #② dip angles position Joint #① closer to excavation boundaries, promoting crack-boundary intersection and potential crack multiplication. Single-length joints exhibit proportional crack length-to-joint size relationships, while mixed-length systems develop complex stress redistribution enabling extended crack propagation. Joint quantity, geometric orientation, and spatial arrangement collectively govern transient unloading-induced crack evolution and instability mechanisms.

4 NUMERICAL SIMULATION OF TRANSIENT UNLOADING DURING DEEP-BURIED CAVERN EXCAVATION

Existing studies on jointed rock transient unloading primarily addressed joint geometry/spatial configurations, overlooking joint material heterogeneity. This chapter employs finite element analysis with an implicit-explicit-implicit sequential method to investigate deformation-damage mechanisms in surrounding rock during transient unloading, including systematic analysis of unloading rate effects.

4.1 Model Establishment

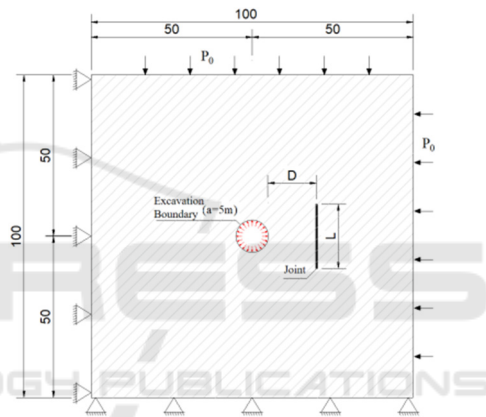


Figure 9: Schematic Diagram of Transient Unloading Model for Jointed Rock Masses.

The jointed rock mass model (100 m × 100 m) features a central excavation cavity ($a=5$ m) for simulating excavation-induced transient unloading. Plane strain conditions are enforced through displacement constraints on front/rear surfaces, with peripheral non-reflective boundaries for wave reflection suppression. A 40 MPa global load simulates in-situ stress. Initial equilibrium is established by applying radial confinement equivalent to in-situ stress at cavity periphery ($t=0$), followed by linear unloading to 0 MPa to replicate blasting-induced transient stress release. The geometric configuration and staged loading protocol are illustrated in Figure 9.

4.2 Influence Mechanisms of Joint Stiffness on Surrounding Rock Deformation and Damage During Transient Unloading

Subsequent numerical simulations focus on the damage and deformation characteristics of surrounding rock under varying joint stiffness conditions. In practical engineering, rock masses typically contain both persistent and non-persistent joints. However, this study exclusively addresses non-persistent joints, as under high in-situ stress conditions, joints are predominantly closed, with normal stiffness values generally ranging between $kn=0.05E$ and $kn=0.2E$ (2018; Zhu et al., 2014; Dai & Zhang, 2012). Accordingly, joint normal stiffness values are set to $kn=0.05E$, $0.10E$, $0.15E$, $0.20E$, and $0.25E$, while tangential stiffness is fixed at 20% of the normal stiffness ($ks=0.2kn$).

Figure 10 clearly illustrates the influence of joint stiffness on cavern convergence displacement in short-joint configurations, showing that under short-joint conditions, the maximum convergence displacements occur within the 70° – 80° sector relative to the cavern, with a slight reduction (0.27 cm) as joint stiffness increases from $kn=0.05E$ to $kn=0.25E$. Notably, an anomalous displacement behavior is observed along the horizontal axis closest to the joints, where convergence displacement increases by 0.70 cm during the same stiffness escalation, indicating a counterintuitive stiffness-dependent response.

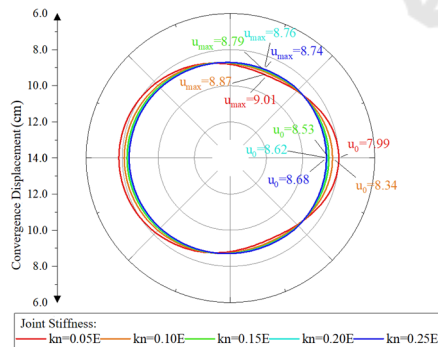


Figure 11: Peripheral Displacement Diagrams of Cavern under Different Joint Normal Stiffness.

The influence of joint stiffness on damage evolution is also significant, as demonstrated in Figure 1, which presents damage contours of short joints under varying joint stiffness conditions. As joint stiffness increases, stress wave reflection diminishes, leading to a reduction in the displacement

differential between reflection and incidence zones. Consequently, the damage severity at joint tips decreases markedly, with the damage zone extent shrinking significantly and gradually disconnecting from the cavern periphery. Similarly, the damage intensity near the cavern, particularly on the side adjacent to the joints, is notably reduced with increasing joint stiffness due to weakened reflection effects.

Joint stiffness exerts relatively minor influence on peripheral displacement and damage. When kn increases from $0.05E$ to $0.25E$, the maximum convergence displacement decreases by only 0.27 cm, while damage zones at joint tips transition from persistent to non-persistent states. In joint support design, a "zoning control strategy" should be adopted: implementing stiffness reinforcement in main displacement zones while coordinating flexible supports in near-field horizontal regions to create mechanical buffer belts.

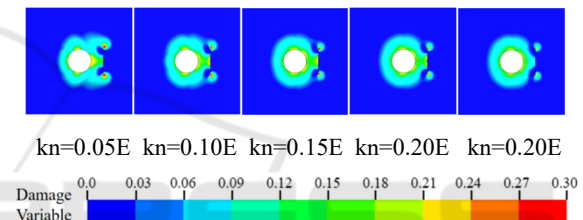


Figure 12: Damage Contours of Surrounding Rock under Different Joint Stiffness Conditions.

5 CONCLUSIONS

The self-developed roadway surrounding rock excavation unloading model test system was employed to simulate instantaneous failure of surrounding rock during tunnel excavation, yielding the following conclusions:

- (1) Model tests revealed that both intact and jointed rock masses develop inverted “八”-shaped cracks under excavation unloading. Compared to intact rock masses, prefabricated jointed rock models exhibit more pronounced crack propagation.
- (2) When multiple joints of equal length exist in a single model, the number of formed cracks aligns closely with the original prefabricated joint count. Longer prefabricated joints result in longer final crack lengths.
- (3) Rock mass models containing prefabricated joints with varying lengths and dip angles demonstrate significant uncertainty in the quantity, length, and

orientation of final cracks, necessitating further systematic investigation.

(4) The coupled "damage suppression-displacement excitation" effect induced by joint stiffness on surrounding displacement and damage of underground chambers reveals the dual attributes of rock mass structural stiffness parameters.

ACKNOWLEDGEMENTS

This work is supported by the Foundation of Hubei Key Laboratory of Blasting Engineering (No.BL2021-13), the National Natural Science Foundation of China (Grant No. 52108368, No. 52109165), the Fundamental Research Funds for the Central Universities (WUT: 2024IVA028).

REFERENCES

- 2018, Некоторые основные задачи математической теории упругости. In H. Zhao, T. Fan, & C. Wang (Eds.), Beijing: China Science Publishing& Media Ltd.
- Cai, M., Kaiser, P. K., Morioka, H., Minami, M., Maejima, T., Tasaka, Y. & Kurose, H. (2007). FLAC/PFC Coupled Numerical Simulation of AE in Large-scale Underground Excavations. *International Journal of Rock Mechanics and Mining Sciences*, 44(4), 550-564. <http://doi.org/10.1016/j.ijrmms.2006.09.013>
- Dai, J. & Zhang, L. (2012). *Shuxue Wuli Fangcheng* [Shuxue Wuli Fangcheng]. Southeast University Press.
- Dong, C., Zhao, G., Li, Y., Meng, X., Lu, X. & Zhang, L. (2017). Mechanical properties and failure mechanism of Surrounding Rocks in Deep Circular Tunnel under Excavation Unloading [Mechanical properties and failure mechanism of surrounding rocks in deep circular tunnel under excavation unloading]. *Journal of Mining and Safety Engineering*, 34(3), 511-518, 526
- Fan, Y., Lu, W., Yang, J., Yan, P. & Chen, M. (2015). Attenuation Law of Vibration Induced by Transient Unloading During Excavation of deep Caverns [Attenuation law of vibration induced by transient unloading during excavation of deep caverns]. *Rock and Soil Mechanics*(2), 541-549. <http://doi.org/10.16285/j.rsm.2015.02.033>
- Lu, W. (1996). A Study on Interaction between Stress wave and Slipping rock Interface [A Study on Interaction between stress wave and slipping rock interface]. *Rock and Soil Mechanics*(3), 70-75.
- Lu, W., Zhou, C., Chen, M., Jin, L. & Yan, L. (2008). Research on Transient Characteristics of Excavation Unloading [research on transient characteristics of excavation unloading]. *Chinese journal of rock mechanics and engineering*, 27(11), 2184-2192. <http://doi.org/10.3321/j.issn:1000-6915.2008.11.003>
- Luo, S., Yan, P., Lu, W., Dong, Z., Zhou, C., Yang, Z. & Hu, Y. (2023). Stability Index of Surrounding Rock during Deep Rock Excavation Considering Energy Release Speed. *Applied sciences*, 13(5), 3000. <http://doi.org/10.3390/app13053000>
- W. Lu, M. Chen, P. Yan, & C. Zhou. (2007). Study On Vibration Characteristics of Surrounding rock Induced by Tunnel Excavation under high in-situ stress [study on Vibration Characteristics of Surrounding rock induced by Tunnel Excavation under High in-situ stress]. *chinese journal of rock mechanics and engineering*, 26(z1), 3329-3334. <http://doi.org/10.3321/j.issn:1000-6915.2007.z1.111>
- Yan, P., Lu, P., & Xu, H. (2007). A Primary Study to Damage Mechanism of Initial Stress Dynamic unloading when Excavating Under high geostress condition [A primary study to damage mechanism of initial stress dynamic unloading when excavating under high geostress condition]. *Explosion and Shock WAVES*, 27(3), 283-288. <http://doi.org/10.3321/j.issn:1001-1455.2007.03.016>
- Yang, J. (2014). *Coupling Effect of Blasting and Transient Release of In-situ Stress during Deep Rock Mass Excavation* [Doctor, Wuhan University].
- Zhu, J., Yang, J., Shi, G., Wang, J. & Cai, J. (2014). Calculating method for conformal mapping from exterior of unit circle to exterior of cavern with arbitrary excavation cross-section [Calculating method for conformal mapping from exterior of unit circle to exterior of cavern with arbitrary excavation cross-section]. *Rock and Soil Mechanics*(1), 175-183.